nature communications

Article

https://doi.org/10.1038/s41467-024-51608-y

Proximity induced charge density wave in a graphene/1T-TaS$_2$ heterostructure

Received: 29 May 2024

Accepted: 7 August 2024

Published online: 14 September 2024

Check for updates

Nikhil Tilak [1,8], Michael Altvater [1,8], Sheng-Hsiung Hung [2,8], Choong-Jae Won [3], Guohong Li [1], Taha Kaleem [1], Sang-Wook Cheong [1], Chung-Hou Chung [4,5,6] ✉, Horng-Tay Jeng [2,5,7] ✉ & Eva Y. Andrei [1] ✉

The proximity-effect, whereby materials in contact appropriate each other's electronic-properties, is widely used to induce correlated states, such as superconductivity or magnetism, at heterostructure interfaces. Thus far however, demonstrating the existence of proximity-induced charge-density-waves (PI-CDW) proved challenging. This is due to competing effects, such as screening or co-tunneling into the parent material, that obscured its presence. Here we report the observation of a PI-CDW in a graphene layer contacted by a 1T-TaS$_2$ substrate. Using scanning tunneling microscopy (STM) and spectroscopy (STS) together with theoretical-modeling, we show that the coexistence of a CDW with a Mott−gap in 1T-TaS$_2$ coupled with the Dirac-dispersion of electrons in graphene, makes it possible to unambiguously demonstrate the PI-CDW by ruling out alternative interpretations. Furthermore, we find that the PI-CDW is accompanied by a reduction of the Mott gap in 1T-TaS$_2$ and show that the mechanism underlying the PI-CDW is well-described by short-range exchange-interactions that are distinctly different from previously observed proximity effects.

The isolation and manipulation of atomically thin materials provide a ready-made two-dimensional electron system[1] whose properties can be tuned by external knobs such as stress, substrate morphology, or doping[2–8], to facilitate the emergence of correlated electron phases. Distinct from these external knobs, a powerful approach to manipulate electron correlations is by contact proximity effects. It is well known that proximitizing materials that host correlated electron phases with a normal metal, induces correlations in the metal[9]. This is a consequence of the quantum mechanical properties of electrons in solids; specifically, the non-local nature of electrons. As quantum particles do not have a well-defined position, electronic states cannot abruptly change from one type of ordering to another at the interface between two materials. Thus, correlated states persist into the normal metal where scattering events begin to destroy the coherence (and vice versa). In the case of 2D materials where scattering is reduced due to their atomically sharp interfaces, proximity-effects are particularly robust allowing proximitized states to persist over long distances. The discovery of graphene and other 2D materials, together with technology enabling the fabrication of 2D heterostructures, has led to the observation of strong proximity effects at the atomic limit, including proximity-induced superconductivity, magnetism[10], and spin-orbit effects[11–18].

CDW states[19,20] that are typically induced by Fermi surface instabilities driven by electron-phonon coupling[21] or by correlation-enhanced exchange effects[22,23], are quite robust. By contrast, PI-CDW in contacted 3D metals are fragile and easily destroyed by interface

---

[1] Department of Physics and Astronomy, Rutgers, the State University of New Jersey, Piscataway, New Jersey, USA. [2] Department of Physics, National Tsing Hua University, Hsinchu, Taiwan. [3] Laboratory for Pohang Emergent Materials and Max Plank POSTECH Center for Complex Phase Materials, Department of Physics, Pohang University of Science and Technology, Pohang, Korea. [4] Department of Electrophysics, National Yang Ming Chiao Tung University, Hsinchu, Taiwan. [5] Physics Division, National Center for Theoretical Sciences, Taipei, Taiwan. [6] Center for Theoretical and Computational Physics, National Yang Ming Chiao Tung University, Hsinchu, Taiwan. [7] Institute of Physics, Academia Sinica, Taipei, Taiwan. [8] These authors contributed equally: Nikhil Tilak, Michael Altvater, Sheng-Hsiung Hung. ✉ e-mail: chung0523@nycu.edu.tw; jeng@phys.nthu.edu.tw; eandrei@physics.rutgers.edu

defect scattering. The use of 2D heterostructures fabricated in an inert atmosphere to avoid interface damage and contamination has made it possible to address this difficulty by substantially reducing interface scattering[24,25]. However, unambiguously identifying a PI-CDW in a 2D heterostructure is challenging due to competing mechanisms such as screening, doping, or strain, which can also produce charge modulations. In addition, as is the case of local probes such as STS, co-tunneling into the parent material can obscure the proximity induced CDW. Therefore, in order to demonstrate a PI-CDW one must: (i) demonstrate the presence of a CDW in the contacted material with the same period as that of the parent material (ii) rule out misidentification of electrostatic screening effects as a PI-CDW (iii) rule out misidentification of the parent CDW as the PI-CDW. Thus far studies of 2D heterostructures comprised of graphene and transition metal dichalcogenides (TMD) were unable to satisfy the three necessary criteria to unambiguously demonstrate the existence of a PI-CDW[24–27].

In this work, we present evidence of PI-CDW in a graphene layer contacted by a 1T-TaS$_2$ substrate hosting a commensurate CDW (CCDW). This discovery was made possible by the unique coexistence of the CDW and Mott gap in 1T-TaS$_2$ together with the Dirac spectrum of graphene. This exceptional combination, which was not present in any of the previously studied systems[24–27], enabled us to unambiguously establish the presence of the PI-CDW by ruling out charge density modulations induced by trivial co-tunneling processes or by screening effects. By comparing STM and STS measurements with first-principle calculations as well as with mean-field theory results, we demonstrate that the charge density modulation of the CCDW in 1T-TaS$_2$ persists within the contacted graphene layer. Further, we identify the effect of charge transfer on the band structure of 1T-TaS$_2$ and reveal that the PI-CDW is described by a mechanism of short-range exchange interactions.

Results and discussion

1T-TaS$_2$ is comprised of hexagonal layers of tantalum atoms coordinated octahedrally by sulfur atoms. Below 550 K a high-temperature metallic phase transits into an incommensurate CDW phase, followed by a nearly commensurate CDW (NCCDW) below 350 K, and a CCDW below 180 K[24] (Fig. 1c). The CDW unit cell consists of a 13-atom cluster where 12 atoms displace from their high-temperature equilibrium positions toward the central, 13th Ta atom forming a $\sqrt{13} \times \sqrt{13}$ reconstructed supercell (Fig. 1b) also known as a David star (DS) structure. The CDW in 1T-TaS$_2$ is driven by strong electron-phonon coupling, which critically suppresses an acoustic phonon mode along the Γ-M direction[28,29] (Supplementary Fig. 4) leading to the static displacement of the lattice with the wavevector $\mathbf{Q}_{\mathbf{CDW}}$, corresponding to the $\sqrt{13} \times \sqrt{13}$ CDW. This soft phonon mode consists primarily of longitudinal vibrations of Ta atoms with a minor contribution from transverse vibrations of S atoms relative to the phonon propagating direction $\mathbf{Q}_{\mathbf{CDW}}$. The DS atomic arrangement involves the local lattice contraction around the center of the star, in which the bond lengths between Ta ions are shorter than those between Ta ions outside the DS.

We studied heterostructures of thin 1T-TaS$_2$ flakes (7–50 nm) covered by monolayer graphene (graphene/1T-TaS$_2$) using STM and STS (Fig. 1a). The samples were assembled inside a dry argon-filled

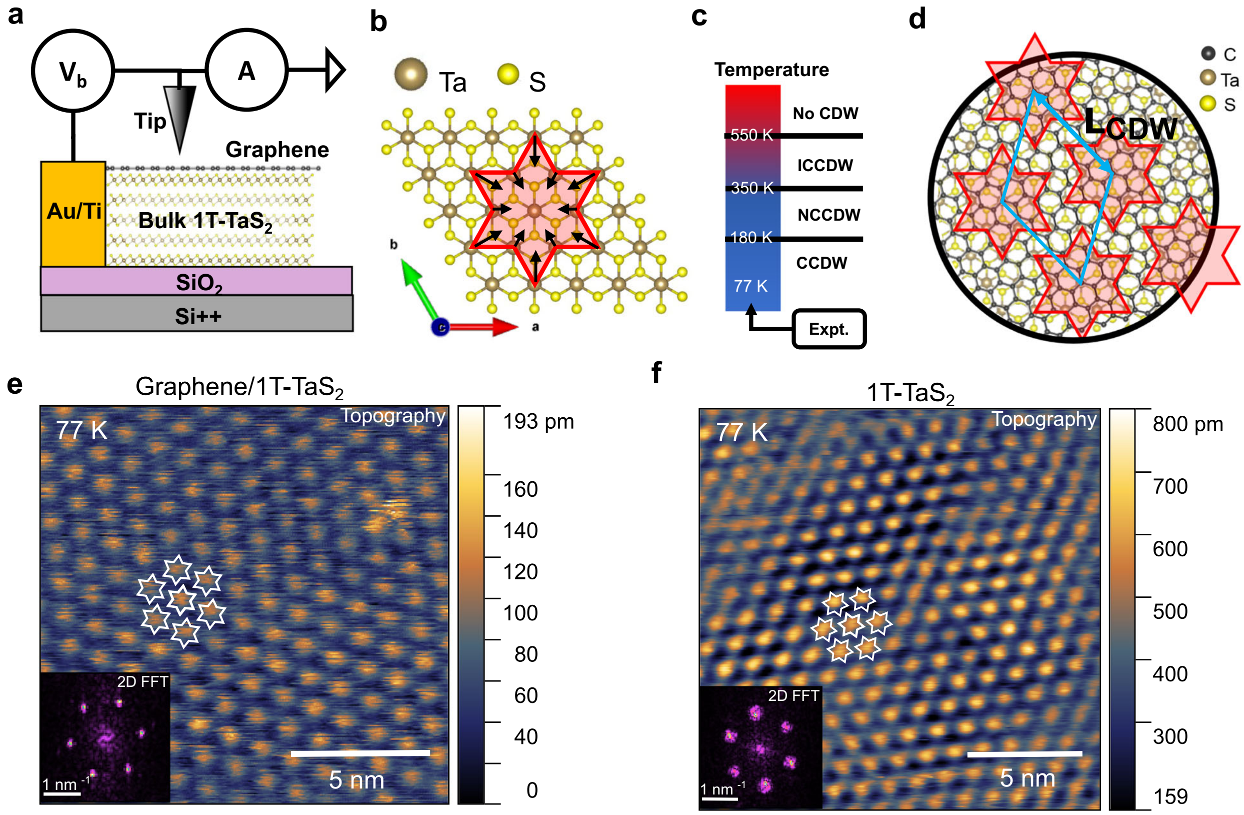

Fig. 1 | Scanning tunneling microscopy of graphene covered 1T-TaS$_2$. **a** Schematic of the device and STM measurement setup. **b** Cartoon showing a single star-of-David (red) in 1T-TaS$_2$. The black arrows denote the displacement of Ta atoms towards a central Ta atom. **c** The transition temperatures between the incommensurate CDW (ICCDW), nearly commensurate CDW (NCCDW), and commensurate CDW (CCDW) phases of 1T-TaS$_2$. **d** Cartoon showing a monolayer graphene layer on top of 1T-TaS$_2$. Here, the angle between the graphene layer and 1T-TaS$_2$ is 13.9° to form a commensurate unit cell (cyan) for DFT calculations. **e** An STM topography image of graphene-covered 1T-TaS$_2$ measured at 77 K using a tunneling set point of $I = 150$ pA, $V_b = 250$ mV. Each bright spot corresponds to a star of David with a measured CDW wavelength of 1.2 nm. This can also be seen in the 2D-FFT of the topography data (inset). **f** An STM topography image and its 2D FFT (inset) of a bulk 1T-TaS$_2$ sample measured at 77 K using a tunneling set point of $I = 150$ pA, $V_b = 500$ mV. The crystals in panels b and d were plotted using VESTA[49].

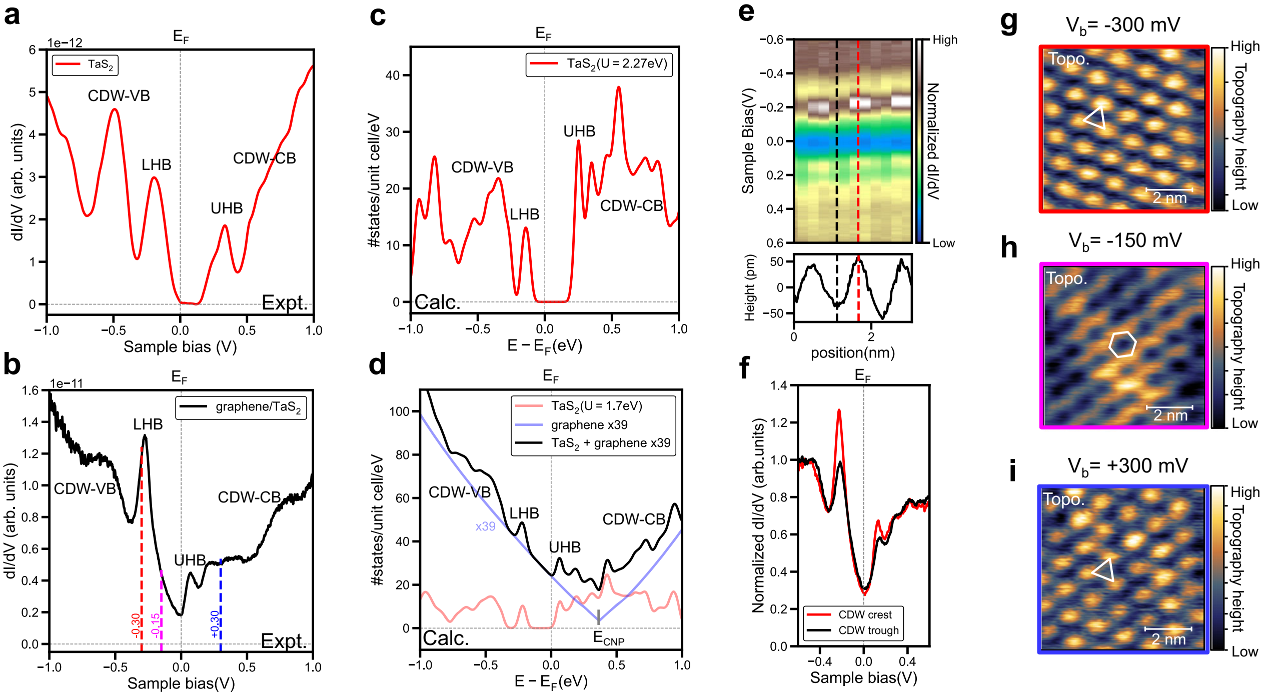

Fig. 2 | Effects of interaction between graphene and 1T-TaS$_2$. **a**, **b** are the measured dI/dV curves on bulk 1T-TaS$_2$ and graphene/1T-TaS$_2$ respectively. The positions of the Hubbard band peaks and the broad features originating from the CDW distortion are labeled. The red, magenta, and blue dashed lines in (**b**) indicate the bias voltages at which topography scans (**g**–**i**) were measured, respectively. **c** The calculated DOS for bulk 1T-TaS$_2$. **d** The calculated DOS for the heterostructure decomposed into the partial DOS of graphene (blue curve) and 1T-TaS$_2$ (red curve). The graphene DOS is multiplied by a factor (39) before adding the 1T-TaS$_2$ DOS (black curve) for comparison with the experiment. This accounts for the smaller tip-graphene separation. See SI for how the factor was estimated. The linear dispersion around the Dirac point of graphene at ~ 0.3 eV above E_F indicates charge transfer from graphene to 1T-TaS2. **e** A map of *dI/dV* (V_b) vs position across 8 DSs in graphene/1T-TaS$_2$. The intensity of both Hubbard bands is highest at the center of the DSs. **f** Three representative spectra from the map in (**e**) demonstrate this intensity variation. **g**–**i** STM topography scans measured at bias voltages of − 300 mV, − 150 mV, and + 300 mV respectively indicated by dashed lines in (**b**). The tunneling resistance was kept constant at 1 GΩ for all scans. The small lateral mismatch between scans is a result of the thermal drift of the sample. All scale bars are 2 nm.

glovebox (< 0.1 ppm O_2, H_2O)[24,30] to avoid oxidation of the air-sensitive surface of 1T-TaS$_2$ and subsequently cooled to 77 K inside a home-built STM[31,32]. At this temperature, 1T-TaS$_2$ is in the CCDW regime. The STM topography (Fig. 1e) measured on a graphene/1T-TaS$_2$ sample using a positive bias set-point (V_b = 250 mV) shows a triangular array of tall spots. The lattice spacing for this array is about 1.2 nm as measured directly from the topography image and confirmed with its fast Fourier transform (FFT) (Fig. 1e, inset). This spacing is equal to the expected CDW wavelength (L_{CDW}) in 1T-TaS$_2$ indicating that each tall spot corresponds to one DS. The topography of the graphene-covered sample thus reflects the distinct arrangement of the DS clusters which are the hallmark of the CDW in 1T-TaS$_2$[33]. The topography is identical to that measured on a bulk 1T-TaS$_2$ sample without a graphene cover under similar tunneling conditions (Fig. 1f). This result also holds true for negative bias set points of $V_b < -300$ mV. In other words, for sufficiently large bias voltages, of either sign, there is no noticeable difference in the STM topography of 1T-TaS$_2$ with or without a graphene cover. This similarity might suggest that there is little or no interaction between the two materials. However, spectroscopy and low bias-voltage topography scans show that this is not the case.

The high-temperature band structure of bulk 1T-TaS$_2$ consists of an isolated, half-filled spin-degenerate flat band at the Fermi level (E_F) (Supplementary Fig. 5). In the CCDW phase, the flat band splits into an occupied spin up lower Hubbard band (LHB) and empty spin down upper Hubbard band (UHB) with a Mott gap of ~ 0.5 eV in between (ab initio calculation Fig. 2c). The other bands corresponding to the CDW distortion appear at energies below the LHB (CDW-VB) and above the UHB (CDW-CB). These spectroscopic features are clearly observed in the experimental *dI/dV* spectrum (Fig. 2a) measured on a bulk 1T-TaS$_2$ sample, in agreement with previous reports[20,23,34,35].

The spectral features of graphene/1T-TaS$_2$ (Fig. 2b), like those of bare 1T-TaS$_2$, show two peaks at ~ − 270 meV and + 70 meV, identified as the LHB and UHB respectively. This identification is supported by the intensity variation of these features as a function of distance from the DS centers (Fig. 2e, f). The main differences between the 1T-TaS$_2$ and graphene/1T-TaS$_2$ spectra are the shift of the Fermi level and the linearly dispersing states within the Mott gap. The former can be understood in terms of the interfacial charge transfer caused by the work function difference between graphene (Φ_G ~ 4.6 eV[36]) and 1T-TaS$_2$ ($\Phi_{1T\text{-}TaS2}$ ~ 5.2 eV[37]). Consequently, the Fermi level moves from the LHB top to the UHB bottom, while the graphene Dirac point shifts to a higher energy of about 0.3 eV above E_F, indicating hole doping. The linearly dispersing Dirac cone states give rise to a linear band within the Mott gap of the 1T-TaS$_2$. While the DFT model reproduces the presence of graphene-attributed density of states at the Fermi level, we find that the experimental *dI/dV* spectrum at higher energies is qualitatively different from the calculated DOS. The discrepancy arises from the exponential sensitivity of the signal on the distance between the STM tip and electronic states within the sample structure. Taking into account the decay of the wavefunction from the graphene surface to the 1T-TaS$_2$ substrate, we find that the contribution of the graphene layer to the calculated DOS should be multiplied by ~ 39 compared to that of the 1T-TaS$_2$ layer (Supporting Information). The weighted sum (black) of the projected DOS of 1T-TaS$_2$ and that of graphene multiplied by 39 (blue) reproduces the asymmetric V-shaped DOS measured experimentally (Fig. 2d). While STM measurements of van der Waals heterostructures are common, de-convolving the

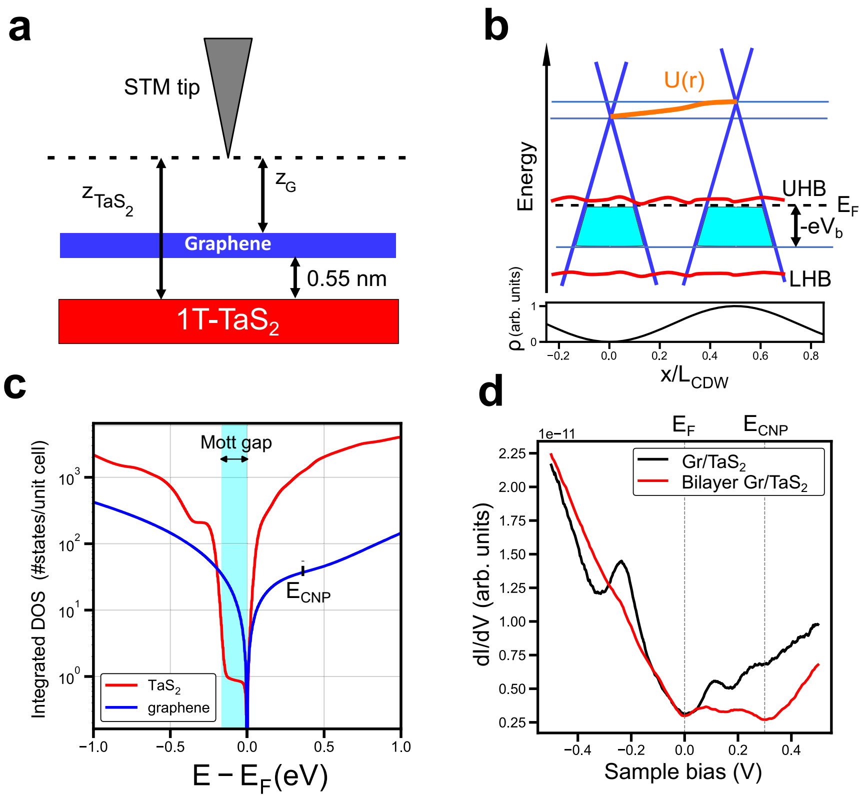

Fig. 3 | Modeling co-tunneling and electrostatic screening. a A schematic cross-section of the tunneling junction. The mean graphene-1T-TaS2 separation is ~ 0.55 nm. Co-tunneling into the graphene and 1T-TaS2 layers was estimated by measuring the tunneling current decay constant z_O. **b** The integrated DOS of the graphene (blue curve) and the 1T-TaS$_2$ (red curve) in the energy window *[E_F, $E_F + eV_b$]* were calculated using the DOS from DFT calculations. The integrated DOS for 1T-TaS$_2$ is about an order of magnitude larger than that of graphene for large V_b. For V_b inside the Mott gap, the graphene DOS dominates. **c** A schematic that considers the effect of screening of the CDW in 1T-TaS$_2$ by the electrons in graphene. The bottom subplot shows the electron density (ρ) in the 1T-TaS$_2$ as a function of position. The resulting electric potential ($U(\mathbf{r})$) denoted by the orange line, tunes the local charge density of the graphene layer. This is denoted by the shift of the charge neutrality point of graphene's Dirac cones (blue) at two representative positions. The Fermi level is denoted by the dashed black line. The red squiggly lines denote the Hubbard bands of the 1T-TaS$_2$. The cyan region shows the states within the energy window *[E_F, $E_F + eV_b$]* for the two positions. There are more states available for tunneling in the graphene above the center of the DSs compared to the sides. This should result in a triangular CDW like pattern in topography measured at these tunneling conditions. This is at odds with the observed hexagonal honeycomb pattern. **d** A *dI/dV* spectrum measured on a bilayer graphene/1T-TaS$_2$ area which shows that the CNP is clearly around 0.3 eV. The Hubbard bands are greatly suppressed compared to the monolayer graphene/1T-TaS$_2$ owing to the increased separation of the topmost graphene layer from the 1T-TaS$_2$, additional screening, and the lack of direct hybridization between the two materials.

different layer contributions to spectroscopy is not. Our procedure provides a computational method to accurately simulate STS measurements of 2D material heterostructures based on DFT models.

Another notable difference between the 1T-TaS$_2$ and the graphene/1T-TaS$_2$ spectra is that the separation between the Hubbard peaks in graphene/1T-TaS$_2$ (~ 338 mV) is smaller by about 31% compared to the bare 1T-TaS$_2$ (~ 491 mV). We attribute this to the reduction of the on-site Coulomb repulsion (U) in the graphene/1T-TaS$_2$ sample due to screening by the highly mobile carriers in graphene. These carriers suppress the localized picture of the narrow Hubbard d-bands in 1T-TaS$_2$ and thus reduce the on-site U value of Ta. Comparing the ab initio calculated band structures (supplementary Fig. 6) for different U values with the STS results suggests that the Hubbard U is lowered from 2.27 eV to 1.70 eV. Using $U = 1.70$ eV in our ab initio calculations (Fig. 2d) we find that the calculated DOS reproduces the main features of the observed STS. Our observation reveals important microscopic details about the effect of screening on correlated insulators that were not initially captured by the DFT model. Similar discrepancies between the measured and calculated DOS in heterostructures of graphene and sister TMDs (1T-NbSe$_2$ and 1T-TaSe$_2$[38–43]) may be resolved by taking into account the screening effects of the conducting substrates.

In addition to the local height variation in the sample, STM topography also depends on the total number of states in the energy window [E_F,$E_F + eV_b$]. For CDW materials, the local DOS variation dominates the topography signal. Since the integrated DOS of 1T-TaS$_2$ is orders of magnitude larger than that of graphene for large V_b (Fig. 3b), we estimate that there is substantial tunneling current into both the graphene and 1T-TaS$_2$, despite the larger z separation between the tip and the 1T-TaS$_2$ layer (Fig. 3a). Consequently, at high bias voltages the topography scans on graphene/1T-TaS$_2$ resemble those on 1T-TaS$_2$, as shown for $V_b = -300$ mV (Fig. 2g) and $V_b = +300$ mV (Fig. 2i). Note that these two energy windows include the LHB and UHB of the 1T-TaS$_2$, respectively.

Surprisingly, the topography pattern measured at bias voltages within the Mott gap of 1T-TaS$_2$ is hexagonal instead of the triangular pattern observed outside the Mott gap, but with the same period (Fig. 2h). We note that for bias voltages within the Mott gap of 1T-TaS$_2$, the STM topography includes only states belonging to graphene (Fig. 3b) because tunneling into the 1T-TaS$_2$ layer is disallowed. Therefore, since a hexagonal lattice is the dual of a triangular lattice, we conclude that the electronic density redistribution in graphene due to its proximity to 1T-TaS$_2$ forms a CDW pattern which is out-of-phase with the CDW in the underlying 1T-TaS$_2$. This result excludes an interpretation of the data in terms of co-tunneling into the 1T-TaS$_2$ substrate. The hexagonal pattern was observed for multiple energy windows inside the 1T-TaS$_2$ Mott gap but never outside it (Supplementary Fig. 10)

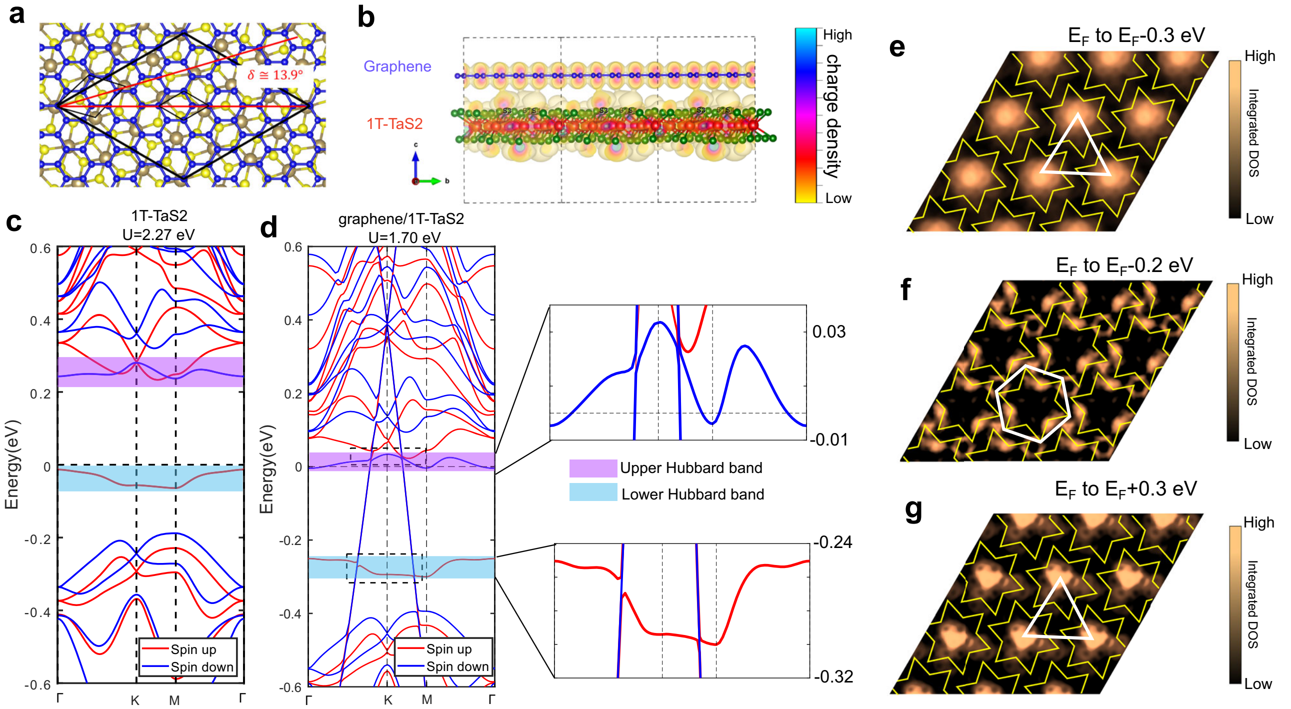

Fig. 4 | Ab initio band structure calculations. a Top view of graphene/1T-TaS_2. Blue, brown, and yellow spheres indicate C, Ta, and S atoms, respectively. Black, blue, and brown rhombuses show the 5 × 5 graphene/√13 × √13 1T-TaS_2 supercell, graphene 1 × 1 unit cell, and 1T-TaS_2 1 × 1 unit cell, respectively. The calculations were carried out for a ~ 13.9° twist angle between graphene and 1T-TaS_2. **b** Side view of graphene/1T-TaS_2 overlaid with the charge density map (bubble-shaped color contour indicating the electron density) corresponding to the states at the two crossing points of the Dirac cone and Lower Hubbard band. The slight overlap between graphene and 1T-TaS_2 electron clouds gives rise to the interlayer coupling and proximity effect. Here, blue, red, and green spheres represent C, Ta, and S atoms, respectively. **c** GGA + U spin resolved band structure of √13 × √13 CDW reconstructed 1T-TaS_2 with $U = 2.27$ eV. **d** GGA + U spin resolved band structure of graphene/1T-TaS_2 using the phenomenological value $U = 1.70$ eV. The red and blue curves are the spin-up and down bands, respectively. Owing to the charge transfer from graphene to 1T-TaS_2, the Fermi level (zero energy) moves from the lower Hubbard band to the upper Hubbard band, and the graphene-associated Dirac point is shifted to ~ 0.3 eV above the Fermi level indicating hole doping. Insets on the right are zoomed in views of the bands near the upper and lower Hubbard bands. **e**–**g** The integrated DOS of graphene/1T-TaS_2 in the energy range from E_F to − 300 mV, − 200 mV, and + 300 mV, respectively, relative to that of freestanding graphene in corresponding energy ranges. DSs are overlaid for clarity. For the energy above the UHB (**e**) and below the LHB (**g**), the integrated DOS forms a triangular lattice. While within the Mott gap (**f**), the in-gap DOS forms a hexagonal lattice, in good agreement with our experimental observations in Fig. 2(g–i).

Note that this out-of-phase CDW cannot be explained by a simple screening picture (Fig. 3c). To wit: if one models the CDW in 1T-TaS_2 as a periodic modulation of electron density ($\rho(r)$) which peaks at the center of the DSs (Fig. 3c, bottom), then the electrostatic potential ($U(r)$) near the surface of 1T-TaS_2 will also peak near the center of the DSs (orange line in Fig. 3c). A graphene layer placed on top of 1T-TaS_2 will experience this spatially varying potential leading to spatial doping variation, i.e., shifting of the local CNP. This CNP variation is in addition to the average shift of the CNP (~ 0.3 eV) due to the work function difference between the two materials as discussed above. If we consider an energy window in the Mott gap of the 1T-TaS_2, then there are more graphene states (cyan regions in Fig. 3b) near the center of the DS compared to the region between neighboring DSs. This should result in a triangular CDW pattern in STM topography, which is in phase with the underlying 1T-TaS_2 CDW. This is contrary to our observation of a hexagonal pattern, thus ruling out this simple picture. These results provide strong evidence for the existence of a PI-CDW in graphene.

We also studied an area of the sample covered with bilayer graphene. In this area, the topography showed almost no CDW pattern. *dI/dV* spectra (Fig. 3d) showed a bilayer graphene-like V shape with a pronounced dip near 0.3 V, indicating the CNP. Very weak features corresponding to the position of the Hubbard bands were also seen. These observations indicate that the PI-CDW relies on very short-range coupling between the graphene and 1T-TaS_2.

We performed first-principle electronic structure calculations using the projector augmented wave (PAW) approach within the framework of density functional theory (DFT) as implemented in the Vienna ab initio Simulation Package (VASP)[44,45]. The exchange-correlation is described in the Perdew-Burke-Ernzerhof (PBE) form of generalized gradient approximation (GGA)[46,47]. To take the strong correlation of Ta d-electrons into consideration, we perform GGA plus on-site U (GGA + U) calculations with $U = 2.27$ eV for monolayer 1T-TaS_2 in accordance with previous DFT calculations[33,48]. The lattice structure is theoretically optimized with the atomic forces converging within 0.01 eV/Ang.

Next, we calculated the GGA + U band structure of a monolayer 1T-TaS_2 covered with graphene using the reduced value $U = 1.7$ eV (Fig. 4d) to reproduce the observed spacing between the Hubbard bands. To enable this calculation, we considered a twist angle of 13.9 degrees between the graphene and 1T-TaS_2 layers. This forms a commensurate superstructure (Fig. 4a) because $5 \times a_G \approx L_{CDW}$, where $a_G = 0.246$ nm is the lattice constant of graphene (Supplementary Fig. 8). We note that both the 1T-TaS_2 Hubbard bands and the graphene Dirac cone are preserved (Fig. 4d) in the band structure. At the intersections between the Dirac cone with the Hubbard bands, four small gaps of ~ 10 meV emerge (Fig. 4d insets). These gaps, which originate from the weak interlayer couplings, indicate finite hybridization between the Dirac and Hubbard states, giving rise to the proximity effect between graphene and 1T-TaS_2 as illustrated in Fig. 4b. In addition, we found a gap associated with the CDW distortion (SI Fig. 9), which was too small (~ 1.7 meV) to detect experimentally.

Since different carbon atoms in the heterostructure unit-cell have a different registry with respect to the underlying CDW, it is natural to expect that the hybridization between graphene p_z-bands and 1T-TaS$_2$ *d*-bands varies as a function of position within the supercell. This can be seen in the calculated charge density map (Fig. 4b). To show the charge modulation of graphene in the proximity CDW state (Fig. 4e–g) for comparison with the experimental topography maps (Fig. 2h–g), we calculate the integrated DOS in the energy windows $[E_F, E_F + eV_b]$ for $V_b = -0.3$ V, − 0.2 V and + 0.3 V by subtracting the counterparts of freestanding graphene in the corresponding energy ranges, i.e., in the energy windows [− 0.3 eV, − 0.6 eV], [− 0.3 eV, − 0.5 eV] and [− 0.3 eV, 0.0 eV] with 0.0 eV being the Dirac point (E_F) of freestanding graphene. Consistent with the experimental results, we find triangular, hexagonal, and triangular CDW patterns below, within, and above the Mott gap region, respectively, providing further support for the out-of-phase PI-CDW in the graphene layer.

The PI-CDW is an effect driven by periodically varying band hybridization. In addition to the DFT calculations, we further modeled the graphene/1T-TaS$_2$ system using a simplified mean-field Hamiltonian (detailed in the SI) based on the existing CDW order in 1T-TaS$_2$ with a weak charge transfer between the graphene and 1T-TaS$_2$ layers. The charge transfer is described by a short-ranged exchange term produced by second-order perturbation of the weak interlayer hopping. Using a mean-field decoupling of this exchange term, a PI-CDW order (much weaker than that in 1T-TaS$_2$), is generated in the graphene layer. We find that the CDW in graphene is out of phase with that in the 1T-TaS$_2$ layer, consistent with both the DFT and the experimental results. In addition, the mean-field theory predicts that the amplitude of the CDW in graphene is much weaker than that in 1T-TaS$_2$, again consistent with the DFT and the STM results. These findings provide strong support for the CDW proximity effect in graphene. We emphasize that the above mechanism based on charge transfer is distinct from previously realized proximity effects, including superconducting, magnetic, and spin-orbit proximity effects.

In summary, using STM/STS together with DFT calculations and mean field Hamiltonian to study graphene/1T-TaS$_2$, we demonstrated the existence of a PI-CDW in graphene and elucidated details of the coupling between the two systems. This was made possible by the unique properties of these two materials, the coexistence of the CDW and Mott gap in 1T-TaS$_2$ together with the Dirac spectrum of electrons in graphene, which enabled us to distinguish the PI-CDW in graphene from the contribution of the host CDW, as well as to rule out a screening-induced charge modulation. We propose a model based on the short-range exchange interaction between carriers in graphene and in 1T-TaS$_2$ which captures the main features of the CDW proximity effect. Concomitant with the PI-CDW in graphene, we observe a reduction in the Mott gap in 1T-TaS$_2$, indicating the presence of proximity-induced mid-gap carriers that screen the Mott–Hubbard interaction. The graphene/1T-TaS$_2$ system provides a sensitive and discriminating probe of contact-induced contributions such as charge transfer, screening, and exchange interactions at the atomic level. Future studies using techniques such as STM/STS and spin-resolved STM to focus on these effects in heterostructures comprised of TMDs and metallic layers could provide new insights into correlated insulator physics and quantum interactions at vdW interfaces, crucial for identifying emergent phenomena, and for understanding quantum transport through 2D materials embedded in 3D structures.

Methods

Sample fabrication and STM measurements

Samples were fabricated by mechanical exfoliation of graphene and separately 1T-TaS$_2$ flakes inside an argon-filled glovebox. 1T-TaS$_2$ flakes were exfoliated from bulk 1T-TaS$_2$ crystals (samples were purchased from 2D Semiconductors or grown by iodine chemical vapor transport) and transferred onto a passivated SiO$_2$-capped degenerately doped Si wafer. The graphene and 1T-TaS$_2$ flakes were aligned vertically, brought into close contact with micromanipulators under an optical microscope, and then heated to promote adhesion. Standard electron beam lithography and electrode deposition (4–5 nm Ti/40–50 nm Au) were used to make electrical contact with the sample. After removing the PMMA mask, the resulting heterostructure was annealed (180 − 220 °C) in hydrogen/argon (10%: 90%) to remove polymer residues followed by AFM tip sweeping. STM and STS were performed using a homebuilt STM at 77 K in high-vacuum $< 10^{-5}$ Torr. To locate the micron-size samples we employed a technique using the STM tip (mechanically cut Pt/Ir) as a capacitive antenna[32]. Two such samples were measured by STM using several mechanically cut Pt/Ir wire tips. In addition, we also studied a 1T-TaS$_2$ flake transferred to a pre-patterned gold electrode using PDMS polymer. This sample was transferred to the STM system with < 15 mins of exposure to the atmosphere.

Data availability

The experimental data generated in this study have been deposited in the Zenodo database under the accession code https://doi.org/10.5281/zenodo.12745631.

References

1. Geim, A. K. & Grigorieva, I. V. Van der Waals heterostructures. *Nature* **499**, 419–425 (2013).
2. Li, G. et al. Observation of Van Hove singularities in twisted graphene layers. *Nat. Phys.* **6**, 109–109 (2010).
3. Levy, N. et al. Strain-induced pseudo-magnetic fields greater than 300 tesla in graphene nanobubbles. *Science* **329**, 544–547 (2010).
4. Carrillo-Bastos, R. et al. Strained fold-assisted transport in graphene systems. *Phys. Rev. B* **94**, 125422–125422 (2016).
5. Jiang, Y. et al. Visualizing strain-induced pseudomagnetic fields in graphene through an hBN magnifying glass. *Nano Lett.* **17**, 2839–2843 (2017).
6. Cao, Y. et al. Correlated insulator behaviour at half-filling in magic-angle graphene superlattices. *Nature* **556**, 80–84 (2018).
7. Mao, J. et al. Evidence of flat bands and correlated states in buckled graphene superlattices. *Nature* **584**, 215–220 (2020).
8. Andrei, E. Y. & MacDonald, A. H. Graphene bilayers with a twist. *Nat. Mater.* **19**, 1265–1275 (2020).
9. Meissner, H. Superconductivity of contacts with interposed barriers. *Phys. Rev.* **117**, 672–680 (1960).
10. Hauser, J. J. Magnetic proximity effect. *Phys. Rev.* **187**, 580–583 (1969).
11. Zhao, R. et al. Tuning phase transitions in 1T-TaS2 via the substrate. *Nano Lett.* **17**, 3471–3477 (2017).
12. Frano, A. et al. Long-range charge-density-wave proximity effect at cuprate/manganate interfaces. *Nat. Mater.* **15**, 831–834 (2016).
13. Li, A. J., Zhu, X., Stewart, G. R. & Hebard, A. F. Bi-2212/1T-TaS2 Van der Waals junctions: Interplay of proximity induced high-Tcsuperconductivity and CDW order. *Sci. Rep.* **7**, 4639 (2017).
14. Dreher, P. et al. Proximity effects on the charge density wave order and superconductivity in single-layer NbSe2. *ACS Nano* **15**, 19430–19438 (2021).
15. Du, X., Skachko, I. & Andrei, E. Y. Josephson current and multiple Andreev reflections in graphene SNS junctions. *Phys. Rev. B* **77**, 184507 (2008).
16. Heersche, H. B., Jarillo-Herrero, P., Oostinga, J. B., Vandersypen, L. M. & Morpurgo, A. F. Bipolar supercurrent in graphene. *Nature* **446**, 56–59 (2007).
17. Avsar, A. et al. Spin-orbit proximity effect in graphene. *Nat. Commun.* **5**, 4875–4875 (2014).
18. Liang, X. et al. The magnetic proximity effect and electrical field tunable valley degeneracy in MoS2/EuS van der Waals heterojunctions. *Nanoscale* **9**, 9502–9509 (2017).

19. Keimer, B., Kivelson, S. A., Norman, M. R., Uchida, S. & Zaanen, J. From quantum matter to high-temperature superconductivity in copper oxides. *Nature* **518**, 179–186 (2015).
20. Lin, H. et al. Scanning tunneling spectroscopic study of monolayerT-TaS 2 and 1 T-TaSe 2. *Nano Res*. **13**, 133–137–133–137 (2020).
21. Johannes, M. D. & Mazin, I. I. Fermi surface nesting and the origin of charge density waves in metals. *Phys. Rev. B* **77**, 165135–165135 (2008).
22. Overhauser, A. W. Exchange and correlation instabilities of simple metals. *Phys. Rev*. **167**, 691–698 (1968).
23. Chen, C.-W., Choe, J. & Morosan, E. Charge density waves in strongly correlated electron systems. *Rep. Prog. Phys*. **79**, 084505 (2016).
24. Altvater, M. A. et al. Charge density wave vortex lattice observed in graphene-passivated 1T-TaS2 by ambient scanning tunneling microscopy. *Nano Lett*. **21**, 6132–6138 (2021).
25. Zhang, Z., Watanabe, K., Taniguchi, T. & LeRoy, B. J. Local characterization and engineering of proximitized correlated states in graphene/NbSe2 vertical heterostructures. *Phys. Rev. B* **102**, 085429 (2020).
26. Rahnejat, K. C. et al. Charge density waves in the graphene sheets of the superconductor CaC6. *Nat. Commun*. **2**, 558–558 (2011).
27. Chen, Y. et al. Visualizing the Anomalous Charge Density Wave States in Graphene/NbSe2 Heterostructures. *Adv. Mater*. **32**, 2003746 (2020).
28. Chen, C., Singh, B., Lin, H. & Pereira, V. M. Reproduction of the charge density wave phase diagram in 1T-TiSe2 exposes its excitonic character. *Phys. Rev. Lett*. **121**, 226602–226602 (2018).
29. Zhang et al. Evidence for a quasi-one-dimensional charge density wave in CuTe by angle-resolved photoemission spectroscopy. *Phys. Rev. Lett*. **121**, 206402–206402 (2018).
30. Altvater, M. A. et al. Observation of a topological defect lattice in the charge density wave of 1T-TaS2. *Appl. Phys. Lett*. **119**, 121601 (2021).
31. Li, G., Luican, A. & Andrei, E. Y. Scanning tunneling spectroscopy of graphene on graphite. *Phys. Rev. Lett*. **102**, 176804 (2009).
32. Li, G., Luican, A. & Andrei, E. Y. Self-navigation of a scanning tunneling microscope tip toward a micron-sized graphene sample. *Rev. Sci. Instrum*. **82**, 073701 (2011).
33. Qiao, S. et al. Mottness collapse in 1T-${\mathrm{TaS_{2-x}}Se_x}$ transition-metal dichalcogenide: An interplay between localized and itinerant orbitals. *Phys. Rev. X* **7**, 041054 (2017).
34. Ma, L. et al. A metallic mosaic phase and the origin of Mott-insulating state in 1T-TaS2. *Nat. Commun*. **7**, 10956 (2016).
35. Wang, Z. et al. Surface-limited superconducting phase transition on 1 T-TaS2. *ACS Nano* **12**, 12619–12628 (2018).
36. Yu, Y.-J. et al. Tuning the graphene work function by electric field effect. *Nano Lett*. **9**, 3430–3434 (2009).
37. Shimada, T., Ohuchi, F. S. & Parkinson, B. A. Work function and photothreshold of layered metal dichalcogenides. *Jpn. j. Appl. Phys*. **33**, 2696–2698 (1994).
38. Chen, Y. et al. Strong correlations and orbital texture in single-layer 1T-TaSe2. *Nat. Phys*. **16**, 218–224 (2020).
39. Liu, Z.-Y. et al. Charge transfer gap tuning via structural distortion in monolayer 1T-NbSe2. *Nano Lett*. **21**, 7005–7011 (2021).
40. Nakata, Y. et al. Robust charge-density wave strengthened by electron correlations in monolayer 1T-TaSe2 and 1T-NbSe2. *Nat. Commun*. **12**, 5873 (2021).
41. Ruan, W. et al. Evidence for quantum spin liquid behaviour in single-layer 1T-TaSe2 from scanning tunnelling microscopy. *Nat. Phys*. **17**, 1154–1161 (2021).
42. Nakata, Y. et al. Monolayer 1T-NbSe2 as a mott insulator. *NPG Asia Mater*. **8**, e321–e321 (2016).
43. Liu, M. et al. Monolayer 1T-NbSe2 as a 2D-correlated magnetic insulator. *Sci. Adv*. **7**, eabi6339 (2011).
44. Kresse, G. Ab initio molecular dynamics for liquid metals. *J. Non Cryst. Solids* **192-193**, 222–229 (1995).
45. Kresse, G. & Furthmüller, J. Efficiency of ab-initio total energy calculations for metals and semiconductors using a plane-wave basis set. *Comput. Mater. Sci*. **6**, 15–50 (1996).
46. Perdew, J. P. et al. Atoms, molecules, solids, and surfaces: Applications of the generalized gradient approximation for exchange and correlation. *Phys. Rev. B* **46**, 6671–6687 (1992).
47. Perdew, J. P. & Wang, Y. Pair-distribution function and its coupling-constant average for the spin-polarized electron gas. *Phys. Rev. B* **46**, 12947–12954 (1992).
48. Darancet, P., Millis, A. J. & Marianetti, C. A. Three-dimensional metallic and two-dimensional insulating behavior in octahedral tantalum dichalcogenides. *Phys. Revi. B* **90**, 045134 (2014).
49. Momma, K. & Izumi, F. VESTA 3 for three-dimensional visualization of crystal, volumetric and morphology data. *J. Appl. Cryst*. **44**, 1272–1276 (2011).

Acknowledgements

N.T. and E.Y.A. acknowledge support from the Department of Energy grant DOE-FG02-99ER45742 and the Gordon and Betty Moore Foundation EPiQS initiative grant GBMF9453; MAA was supported by the National Science Foundation grant EFRI 1433307; G.L. was supported by Rutgers University; C.J.W. was supported by The National Research Foundation of Korea (NRF), Ministry of Science and ICT(No. 2022M3H4A1A04074153); S.W.C. was supported by the Center for Quantum Materials Synthesis (cQMS), funded by the Gordon and Betty Moore Foundation's EPiQS initiative grant GBMF10104, and by Rutgers University, C.-H.C. was supported by MOST (Grant NO.: 107-2112-M-009-010-MY3, 110-2112-M-A49-018-MY3), NSTC (Grant NO. 112-2124-M-A49-003), and NCTS of Taiwan, R.O.C., JHT acknowledges support from the Ministry of Science and Technology, Taiwan under grant: MOST 109-2112-M-007 –034 -MY3, and from NCHC, CINC-NTU, AS-iMATE-109-13, and CQT-NTHU-MOE, Taiwan.

Author contributions

N.T. and M.A. built the STM, performed the experimental studies, and analysis, and wrote the paper; S.-H.H. and H.-T.J. performed the first principles calculations; C.-J.W. grew one of the TaS2 samples; G.L. built the STM and helped with data collection; T.K. helped with sample fabrication; S.-W.C. helped obtain the TaS2 sample; C.-H.C. carried out the mean-field calculations; E.Y.A. directed the project, analyzed data, and wrote the paper.

Competing interests

The authors declare no competing interests.

Additional information

Supplementary information The online version contains supplementary material available at https://doi.org/10.1038/s41467-024-51608-y.

Correspondence and requests for materials should be addressed to Chung-Hou Chung, Horng-Tay Jeng or Eva Y. Andrei.

Peer review information *Nature Communications* thanks the anonymous reviewer(s) for their contribution to the peer review of this work. A peer review file is available.

Reprints and permissions information is available at http://www.nature.com/reprints

Publisher's note Springer Nature remains neutral with regard to jurisdictional claims in published maps and institutional affiliations.

Open Access This article is licensed under a Creative Commons Attribution-NonCommercial-NoDerivatives 4.0 International License, which permits any non-commercial use, sharing, distribution and reproduction in any medium or format, as long as you give appropriate credit to the original author(s) and the source, provide a link to the Creative Commons licence, and indicate if you modified the licensed material. You do not have permission under this licence to share adapted material derived from this article or parts of it. The images or other third party material in this article are included in the article's Creative Commons licence, unless indicated otherwise in a credit line to the material. If material is not included in the article's Creative Commons licence and your intended use is not permitted by statutory regulation or exceeds the permitted use, you will need to obtain permission directly from the copyright holder. To view a copy of this licence, visit http://creativecommons.org/licenses/by-nc-nd/4.0/.

© The Author(s) 2024